JOURNAL OF GEOPHYSICAL RESEARCH: OCEANS, VOL. 118, 4409–4423, doi:10.1002/jgrc.20315, 2013

Processes controlling upper-ocean heat content in Drake Passage

Gordon R. Stephenson Jr.,[1,2] Sarah T. Gille,[1] and Janet Sprintall[1]

Received 18 April 2013; revised 10 July 2013; accepted 11 July 2013; published 13 September 2013.

[1] A 16 year record of expendable bathythermograph transects across Drake Passage is used to examine variability in upper-ocean heat content that is not associated with the annual cycle. Links between upper-ocean heat content and anomalous heat fluxes, winds, two large-scale climate indices, and mesoscale eddies and meanders are examined. Results suggest that interannual variations in surface heat fluxes explain ∼5 to 10% of the variance in upper-ocean heat content. Anomalous surface heat fluxes are linked to meridional wind anomalies upstream of Drake Passage, which in turn are linked to forcing by El Niño/Southern Oscillation (ENSO) and the Southern Annular Mode (SAM). ENSO and SAM are correlated with upper-ocean heat content at near-zero lags, and statistically significant correlations occur at longer time lags as well. The impact of mesoscale eddies and meanders on upper-ocean heat content is explored with the use of a tracked eddy database. An empirical relationship is constructed relating upper-ocean heat content anomalies to eddy length scales and amplitudes. Eddies and meanders are estimated to account for more than one third of the nonannual cycle variance in Drake Passage upper-ocean heat content.

Citation: Stephenson, G. R. Jr., S. T. Gille, and J. Sprintall (2013), Processes controlling upper-ocean heat content in Drake Passage, *J. Geophys. Res. Oceans*, *118*, 4409–4423, doi:10.1002/jgrc.20315.

1. Introduction

[2] Atmosphere-ocean interactions at the sea surface are a primary driver of upper-ocean variability. *Stephenson et al*. [2012] showed that in Drake Passage, surface heat flux forcing accounts for about half of the total variance in heat content within the top 400 m. If half of the variance is associated with the seasonal cycle, then half must be due to processes that are not repeatable on annual timescales, which could be associated either with low-frequency interannual variability or with high-frequency intraseasonal variations. Although *Stephenson et al*. [2012] found that the annual cycle in upper-ocean heat content is well explained by a simple one-dimensional model in which surface heat fluxes balance upper-ocean heat content gains, such a balance does not necessarily apply on other timescales when eddies, frontal meanders, or large-scale climate variability could all play a role [e.g., *Sprintall*, 2003; *Lenn et al*., 2007; *Sprintall*, 2008]. The objective of the present study is to quantify the relative importance of sources of nonseasonal variability in controlling upper-ocean heat content in the Drake Passage region.

[3] Hydrographic data indicate that the Southern Ocean has undergone significant warming in the past five to six decades [e.g., *Böning et al*., 2008; *Gille*, 2008] and suggest that 80% of the observed Southern Hemisphere ocean warming has occurred south of 30°S, within the Southern Ocean [*Gille*, 2008]. Southern Ocean warming has been implicated as a potential source of heat that might contribute to destabilization of the ice shelves around Antarctica and eventually to accelerated sea level rise [e.g., *Jacobs et al*., 2011]. In climate models, projections of global climate change in the coming century depend strongly on how the present-day Southern Ocean takes up heat from the atmosphere [*Boé et al*., 2009]. Thus, the challenge for the present study is to identify the mechanisms that contribute to upper-ocean warming and ocean uptake of heat so that we can better understand the impact on climate in a warming world.

[4] In this study, we focus on Drake Passage, both because it is climatically important, because all circumpolarly transported heat content anomalies must pass through the Drake Passage chokepoint to reach the Atlantic Ocean from the Pacific, and because it is comparatively well sampled by a 16 year near-repeat expendable bathythermograph (XBT) transect, so that we are able to distinguish seasonal from intraseasonal and interannual variability. We explore two types of mechanisms that can control upper-ocean heat content. The first is large-scale processes associated with shifts in wind or buoyancy forcing. The second type of mechanism is associated with individual mesoscale eddies.

[5] On the large scale, we focus on two patterns of interannual variability that are known to have a substantial impact on the Southern Ocean. The Southern Annular

[1]Scripps Institution of Oceanography, University of California, San Diego, La Jolla, California, USA.
[2]Now at School of Ocean Sciences, Bangor University, Menai Bridge, Anglesey, UK.

Corresponding author: G. R. Stephenson Jr., School of Ocean Sciences, Bangor University, Menai Bridge, Anglesey, LL59 5AB, UK. (g.stephenson@bangor.ac.uk)

2169-9275/13/10.1002/jgrc.20315

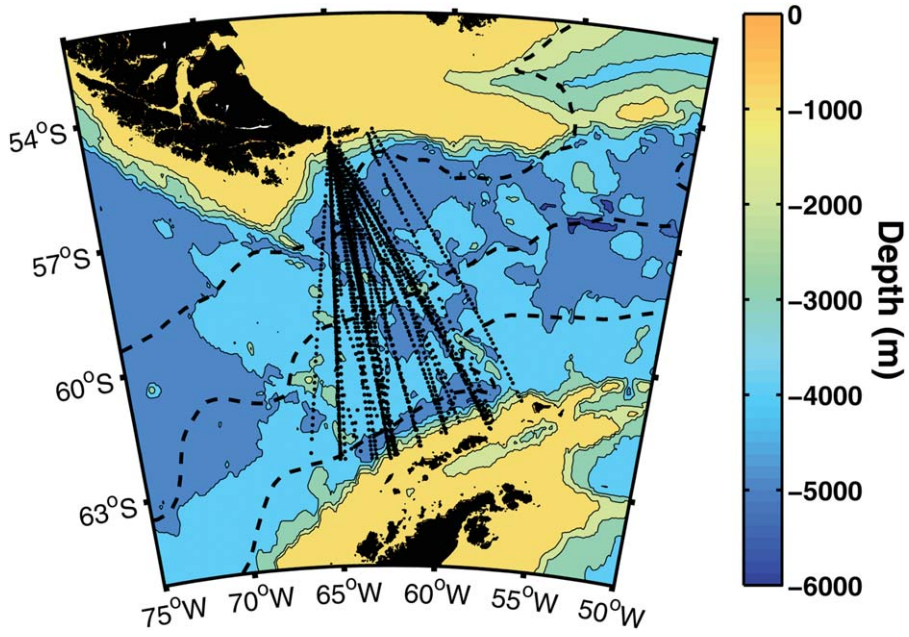

Figure 1. Bathymetric map of Drake Passage showing the locations of XBTs (black dots). The climatologic mean frontal positions [*Orsi et al*., 1995] of (from north to south) the Subantarctic Front, Polar Front, and Southern Antarctic Circumpolar Current Front are indicated (dashed lines).

Mode (SAM), the leading order mode of atmospheric variability in the high-latitude Southern Hemisphere, manifests itself as a strengthening of the meridional pressure gradient around Antarctica [*Thompson and Wallace*, 2000]. With this increase in the sea level pressure gradient comes an intensification and poleward shift of the circumpolar winds [*Hall and Visbeck*, 2002]. Although the SAM has a strong impact over the full circumpolar extent of the Southern Ocean, climate-scale changes in sea surface temperature (SST) in the tropical Pacific also can influence the Southern Ocean. El Niño/Southern Oscillation (ENSO) events lead to atmospheric Rossby wave trains that propagate poleward as alternating cyclonic and anticyclonic atmospheric circulation anomalies [*Turner*, 2004; *Meredith et al*., 2008]. These atmospheric waves affect zonal and meridional surface winds and cloud cover, and thereby influence surface heat fluxes over the Antarctic Circumpolar Current (ACC). The changes in heat flux result in cold SST anomalies near Drake Passage and warm SST anomalies ∼5000 km upstream [*Meredith et al*., 2008]. Advection of the upstream anomalies leads to a positive SST anomaly in Drake Passage ∼2 years later [*Meredith et al*., 2008]. Distinguishing the impacts of ENSO and SAM is somewhat complicated by the fact that they covary: ENSO explains ∼25% of the variance of SAM in austral summer [*L'Heureux and Thompson*, 2006].

[6] In addition, more frequent El Niño (considered here as positive ENSO) events in recent decades [*Trenberth and Hoar*, 1997] and a positive shift in the index of the SAM [*Thompson and Wallace*, 2000] have fueled inquiries into the mechanisms that link large-scale atmospheric forcing to Southern Ocean warming [e.g., *Turner*, 2004; *Meredith et al*., 2008; *Ciasto and England*, 2011]. In the present study, we evaluate the importance of the ENSO-related and SAM-related modes of atmospheric forcing to the overall variability in heat content of the ocean.

[7] The second category of mechanisms that can influence upper-ocean heat content are associated with mesoscale eddies and meanders of the ACC frontal jets. These features are associated with variability occurring largely on higher frequencies, at intraseasonal timescales. Eddies drive poleward heat transport across the ACC fronts [*Böning et al*., 2008], alter local air-sea heat fluxes [*O'Neill et al*., 2003, 2005; *Jiang et al*., 2011], and may also influence local upwelling or downwelling [e.g., *Chelton et al*., 2011a]. In sparsely sampled records, eddy impacts can confound interpretation of large-scale interannual variability that might be associated with the SAM or ENSO teleconnection patterns. For this reason, in the present study we separately assess the impact of individual eddies so as to evaluate their overall contribution to variability of Drake Passage heat content.

[8] This study is organized as follows: section 2 describes the data sets used in this work, and section 3 presents the basic framework used to analyze upper-ocean heat content. Section 4 focuses on heat content variability associated with large-scale SAM- and ENSO-related patterns, e.g., scales that we typically associated with interannual or multiyear variability. Section 5 addresses upper-ocean variability due to eddies and frontal meanders, which we identify from an eddy database developed by *Chelton et al*. [2011b]. In section 6, we discuss the relative contributions of eddies and of variability linked to ENSO and SAM. Finally, section 7 presents a summary and conclusions.

2. Data

2.1. Temperature Transects

[9] The heat content of the upper several hundred meters of the water column is examined with the use of transects

from the Scripps High-Resolution XBT/expendable conductivity, temperature, depth (XCTD) program. Since September 1996, operations on the ASRV (Antarctic Survey and Resupply Vessel) L. M. Gould have included underway deployment of XBTs on six to seven Drake Passage crossings each year (Figure 1). XBT transects across Drake Passage are performed in all seasons. Each transect takes 2–3 days, during which ~70 XBTs are deployed at 10–15 km spacing, or 6–10 km spacing across the Subantarctic and Polar Fronts. The Polar Front is defined here as the northward extent of the 2°C isotherm at 200 m depth [*Orsi et al*., 1995]. XBT probes typically return temperature profiles to their rated depth of 850 m. The fall-rate correction of *Hanawa et al*. [1995] has been applied to each profile. From September 1996 to August 2011, 99 transects were collected. Of these, three transects terminated north of 60°S (September 1997, February 1998, and July 1999) and three transects deviated significantly from the typical crossings shown in Figure 1 (an iceberg was circumnavigated in the September 1999 transect; the transect in June 2000 went much farther east than the rest; the January 2009 transect included a dogleg to the west of the typical crossings). Data from these cruises have been excluded from our analysis. For each of the remaining 93 transects shown in Figure 1, temperature fields from the XBTs have been objectively mapped onto a regular, gridded meridional-depth section with 10 m vertical resolution and 0.1° latitude horizontal spacing [*Sprintall*, 2003]. Where we consider the positions of eddies and meanders in section 5, the longitude of temperature profiles is interpolated from the locations of XBT casts onto the gridded latitude.

2.2. Eddy Database

[10] Sea surface height (SSH) fields can be used to identify mesoscale eddies [e.g., *Sprintall*, 2003; *Fang and Morrow*, 2003; *Isern-Fontanet et al*., 2003]. In the present study, we use the database of eddies identified in weekly gridded AVISO SSH fields by *Chelton et al*. [2011b]. Their algorithm differs from prior methods in that it does not rely on a prespecified threshold in SSH or other parameters to pinpoint eddies. Eddy-like features are included in the database only if they last ≥4 weeks.

[11] The database includes the central latitude and longitude of each eddy, eddy amplitude, and "effective length scale," which is defined as the radius of a circle with an area equal to the area enclosed by a contour of maximum current velocity. Amplitude is given by the difference between the sea surface height anomaly at the center of the eddy and the sea surface height anomaly at the boundary [*Chelton et al*., 2011b]. Thus, cyclonic (cold-core) eddies have a negative amplitude, and anticyclonic (warm-core) eddies have a positive amplitude. Because *Chelton et al*.'s [2011b] database is derived from SSH anomalies, it does not distinguish between transient eddies and frontal meanders, so for the purposes of the present study, we treat eddies and meanders identically. A southward meander of the Polar Front, for example, appears as a large positive anomaly in SSH and has a positive effect on the heat content similar to that of a warm-core eddy.

[12] The eddies in *Chelton et al*.'s [2011b] database were identified with the use of AVISO fields from October 1992 through January 2011, providing information about eddies in all but the three most recent cruises we examined. To identify XBT transects that intersected eddies, we interpolated eddy positions and properties (length scale and amplitude) linearly in time to match the median date of the XBT transect. We classified an eddy as having been sampled if the distance from the eddy center to one or more XBT casts was less than the eddy's effective length scale.

2.3. Heat Fluxes and Wind Fields

[13] The ASRV *L. M. Gould* carries a full suite of meteorologic sensors from which instantaneous heat flux measurements can be made at the time of each XBT drop [e.g., *Jiang et al*., 2011]. For the purposes of the present study, however, we are more interested in the heat fluxes that accumulate between sampling by XBT transects and at a range of distances upstream of Drake Passage. *Stephenson et al*. [2012] examined three heat flux products in Drake Passage: NCEP-NCAR Reanalysis 1 heat fluxes [*Kalnay et al*., 1996], Objectively Analyzed fluxes [*Yu and Weller*, 2007], and Japanese Ocean Fluxes With Use of Remote-Sensing Observations [*Kubota et al*., 2002]. All three were similar on seasonal timescales. For the present study, we used two heat flux products that overlap the entire time span of the XBT transect time series: first, NCEP Reanalysis 2 heat fluxes [*Kanamitsu et al*., 2002], a daily, gridded product with resolution ~1.9° × 1.9° sampled over 1 January 1996 to 31 December 2011; second, ERA-Interim heat fluxes [*Dee et al*., 2011], a daily, gridded product with ~0.75° × 0.75° resolution sampled over the same time period. Heat fluxes in the vicinity of Drake Passage (55–100°W,
54–65°S) were smoothed with a 60-day running mean. Heat flux anomalies (Q'_{net}) were computed relative to a daily climatology of fluxes at each grid point. Our results proved to be insensitive to the choice of heat fluxes; we present only the results from the NCEP Reanalysis 2 heat fluxes.

[14] Interannual variability in wind forcing was explored using wind fields from the NCEP Reanalysis 2 fields [*Kanamitsu et al*., 2002]. The 10-m zonal and meridional components of the wind were smoothed with a 60-day running mean. Wind anomalies were computed relative to a daily climatology at each grid point.

2.4. Climate Indices

[15] For this study, we have focused on large-scale patterns of climate variability as represented by SAM and ENSO indices. To examine the influence of major modes of climate variability, we used lagged correlations of upper-ocean heat content with climate indices. We use a monthly multivariate ENSO index based on principal component analysis of six observed variables in the tropical Pacific [*Wolter and Timlin*, 1998]: sea-level pressure, two components of surface wind, SST, surface air temperature, and cloud fraction. For the SAM index, we use the monthly values based on zonally averaged sea level pressure differences between 40°S and 70°S [*Nan and Li*, 2003].

3. Upper-Ocean Heat Content

[16] Drake Passage is a dynamically active region where transport of ~140 Sv [*Cunningham et al*., 2003; *Firing et al*., 2011] passes through a 700 km wide gap. The strong flow is accompanied by strong temperature gradients at the

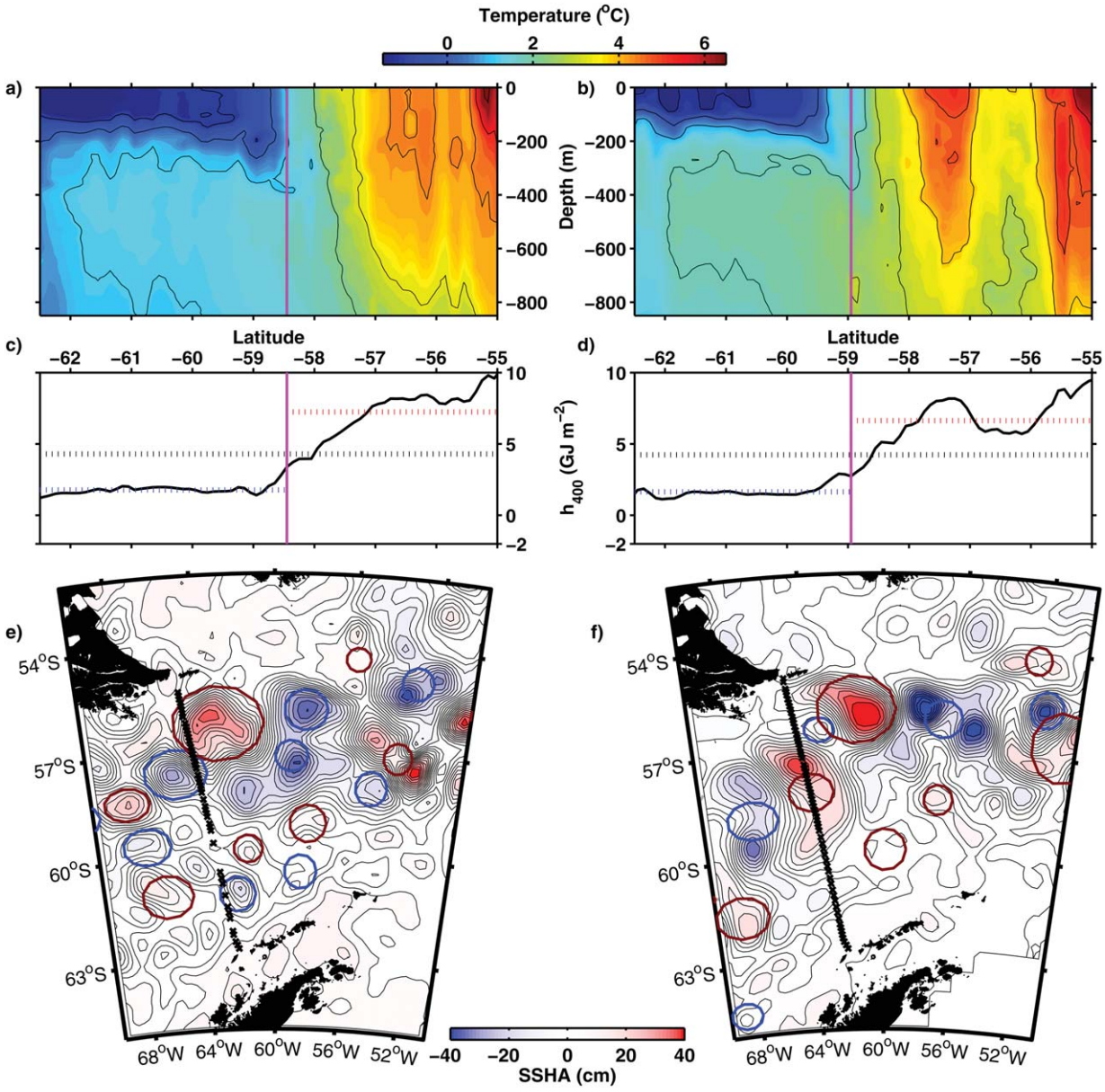

Figure 2. Temperature transects from June cruises in (a) 2006 and (b) 2009. Transects of heat content from 0 to 400 m, h_{400}, across (c) the June 2006 transect and (d) the June 2009 transect with average heat content north of the Polar Front ($\mathcal{H}_N$, red dotted line), south of the Polar Front ($\mathcal{H}_S$, blue dotted line), and over the entire transect ($\mathcal{H}_{400}$, black dotted line). In Figures 2a–2d, the latitude of the Polar Front is indicated by a magenta line. Maps of daily sea surface height anomaly (e) 12 June 2006 and (f) 30 June 2009 and locations of XBT casts (black x). Center location and approximate length scale of cyclonic (blue) and anticyclonic (red) eddies identified in *Chelton et al.*'s [2011b] database.

ACC fronts [*Orsi et al.*, 1995; *Sokolov and Rintoul*, 2009]. The Subantarctic Front, Polar Front, and southern ACC Front divide Drake Passage into regions with very different temperature and density stratifications [*Orsi et al.*, 1995; *Sprintall*, 2003]. South of the Polar Front, cold Antarctic Surface Water (AASW) lies above warmer, more saline Circumpolar Deep Water (CDW; Figures 2a and 2b). North of the Polar Front, temperature stratification is much lower, with near-vertical isotherms possible to depths >800 m (Figures 2a and 2b).

[17] The upper-ocean heat content is a useful measure for understanding upper-ocean variability [e.g., *Willis et al.*, 2004; *Stephenson et al.*, 2012]. In the present study, we define upper-ocean heat content over the upper 400 m of the water column of a single profile, h_{400}, as

$$h_{400}(x,y) = \int_{-400}^{0} \rho_0 c_p T(x,y,z)dz, \qquad (1)$$

where $\rho_0 = 1030\,\mathrm{kg\,m^{-3}}$ is the density of seawater, $c_p = 3985\,\mathrm{Jkg\,m^{-3}}$ is the heat capacity of seawater, and $T(z)$ is

Table 1. Correlations of Upper-Ocean Heat Content with Contributing Terms[a]

	$\mathcal{H}_{400}$	$\mathcal{H}_N$	$\mathcal{H}_S$	ϕ_{PF}
$\mathcal{H}_{400}$	1	0.642[b]	0.681[b]	−0.591[b]
Seasonal cycle	0.705[b]	0.552[b]	0.833[b]	0.311[b]
	$\mathcal{H}'_{400}$	$\mathcal{H}'_N$	$\mathcal{H}'_S$	ϕ_{PF}
$\mathcal{H}'_{400}$	1	0.506[b]	0.292[b]	−0.599[b]
ϕ_{PF}	−0.599[b]	0.037	0.025	1
Q_{55d}	0.436[b]	0.140	0.342[b]	−0.200
$\mathcal{E}$	0.604[b]	0.340[b]	−0.065	−0.420[b]

[a]The upper part of the table shows correlations of the transect-averaged upper-ocean heat content ($\mathcal{H}_{400}$) with average upper-ocean heat content north ($\mathcal{H}_N$) and south ($\mathcal{H}_S$) of the Polar Front and with the latitude of the Polar Front (ϕ_{PF}), as well as the correlation of each variable with its seasonal cycle using a two-harmonic fit. The lower part of the table shows correlations of the residual heat content when a seasonal cycle has been removed ($\mathcal{H}'_{400}, \mathcal{H}'_N, \mathcal{H}'_S$) and ϕ_{PF} with $\mathcal{H}'_{400}, \phi_{PF}$, the average heat flux anomaly upstream of Drake Passage 55 days prior to a transect (Q_{55d}, defined in section 4) and heat content anomaly due to mesoscale eddies and meanders ($\mathcal{E}$, defined in section 5).

[b]Significant correlation.

the temperature at depth z. We select 400 m as an integration depth, because south of the Polar Front temperature variations are small below 400 m, and north of the Polar Front, temperature changes in the top 400 m are strongly correlated with changes in the upper 800 m. In total, *Stephenson et al.* [2012] found that in Drake Passage, more than 75% of upper-ocean thermal variability occurs above 400 m depth.

[18] Two winter (June) transects illustrate year-to-year variability of h_{400} in the region. From 10 to 12 June 2006 (Figure 2a), the Polar Front is found at 58.3°S, whereas from 28 to 30 June 2009 (Figure 2b), the Polar Front is located ~50 km farther south at 58.8°S. The minimum temperature of the AASW is ~0.8°C colder in 2009 than in 2006. The June 2009 transect shows relatively cool 3–4°C water at ~56–57°S latitude, north of the Polar Front. The temperature changes across the Polar Front have a strong signal in h_{400} (Figures 2c and 2d). Both transects pass near or intersect cyclonic (cold-core) and anticyclonic (warm-core) mesoscale features (Figures 2e and 2f). For example, the warm temperatures at 57–58°S in the June 2009 transect (Figures 2b and 2d) may be associated with the warm-core feature centered near 58°S 64°W (Figure 2f).

[19] *Stephenson et al.* [2012] separately considered spatial averages of $h_{400}(x,y)$ over measurements collected north of the Polar Front, $\mathcal{H}_N$, and south of the Polar Front, $\mathcal{H}_S$ (e.g., Figures 2c and 2d). In the present study, we also average $h_{400}(x,y)$ over an entire transect across Drake Passage, denoting the transect-averaged quantity by the upper-case $\mathcal{H}_{400}$ to distinguish transect-averaged heat content from the single-profile values, $h_{400}(x,y)$, used in section 5 to examine mesoscale variability. Thus,

$$\mathcal{H}_{400} = \mathcal{H}_N \frac{\phi_N - \phi_{PF}}{\phi_N - \phi_S} + \mathcal{H}_S \frac{\phi_{PF} - \phi_S}{\phi_N - \phi_S} \qquad (2)$$

where ϕ_N and ϕ_S are the northernmost and southernmost latitudes of the transect, and ϕ_{PF} is the latitude of the Polar Front. Changes in $\mathcal{H}_{400}$ can be associated with $\mathcal{H}_N$ and $\mathcal{H}_S$ or with shifts in ϕ_{PF}. A northward shift in the Polar Front, for example, increases the amount of cold water present in Drake Passage, but does not necessarily imply a change in properties of the water masses that define the Polar Front. By partitioning variability this way, we can estimate how much heat content variability is due to water masses warming or cooling and how much is due to poleward shifts in the location of the front. The northern endpoint of the transects ϕ_N is roughly constant at 54.5°S, because the L. M. Gould always departs from and returns to Punta Arenas, Chile. The southern endpoint, ϕ_S, varies depending on the ship's specific destination in Antarctica (Figure 1). To limit variation in ϕ_N and ϕ_S, we have restricted the latitude range of this study to 54.5°S to 62.5°S; small variations in ϕ_S and ϕ_N occur where transects are terminated within this range. For the 93 Drake Passage transects, $\mathcal{H}_N, \mathcal{H}_S$, and ϕ_{PF} (as in equation (2)) each contribute roughly one third of the variability in $\mathcal{H}_{400}$ (Table 1).

[20] To define heat content anomalies associated with interannual variability, we remove a seasonal cycle from the transect-averaged heat content (Figure 3). A least-squares fit was made to annual and semiannual harmonics; this fit explained ~50% of the variability in $\mathcal{H}_{400}$. Similarly constructed fits explain ~30 and ~70% of the variability in $\mathcal{H}_N$ and $\mathcal{H}_S$, respectively (Table 1). The residuals left when seasonal cycles are removed are denoted $\mathcal{H}'_{400}$ (Figure 3), $\mathcal{H}'_N$, and $\mathcal{H}'_S$. We note that $\mathcal{H}'_S$ has a standard deviation ($0.37\,\mathrm{GJ\,m^{-2}}$) half as large as that of $\mathcal{H}'_N$ ($0.68\,\mathrm{GJ\,m^{-2}}$). Movements of the Polar Front explain ~34% of the interannual variability in $\mathcal{H}'_{400}$, whereas $\mathcal{H}'_N$ explains ~26% of the variance in $\mathcal{H}'_{400}$ and $\mathcal{H}'_S$ explains only 9% of the variance in $\mathcal{H}'_{400}$ (Table 1). This implies that on interannual timescales, changes in water temperature south of the Polar Front contribute less to the overall variability of upper-ocean heat content in Drake Passage than shifts in the Polar Front location and changes in heat content north of the Polar Front. This is not surprising, because changes in temperature south of the Polar Front may be suppressed by heat used in the ice formation/melt cycle.

4. Variability Due to Atmospheric Forcing

[21] This section examines contributions to interannual upper-ocean heat content variability arising from changes in surface heat input and links heat flux anomalies to meridional

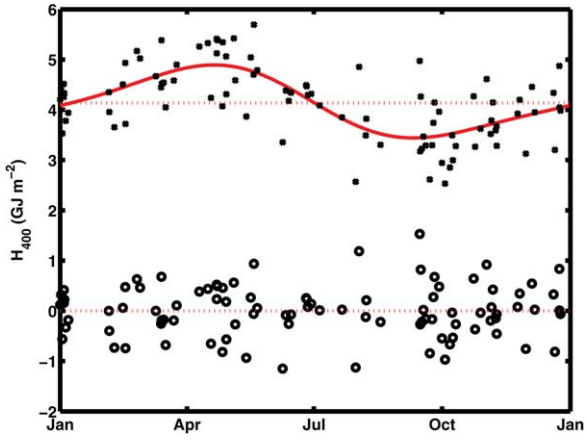

Figure 3. Transect-averaged $\mathcal{H}_{400}$ (black asterisks) and an annual cycle fitting an annual and semiannual cycle (red curve). $\mathcal{H}'_{400}$ (black circles) are the residuals relative to the annual cycle.

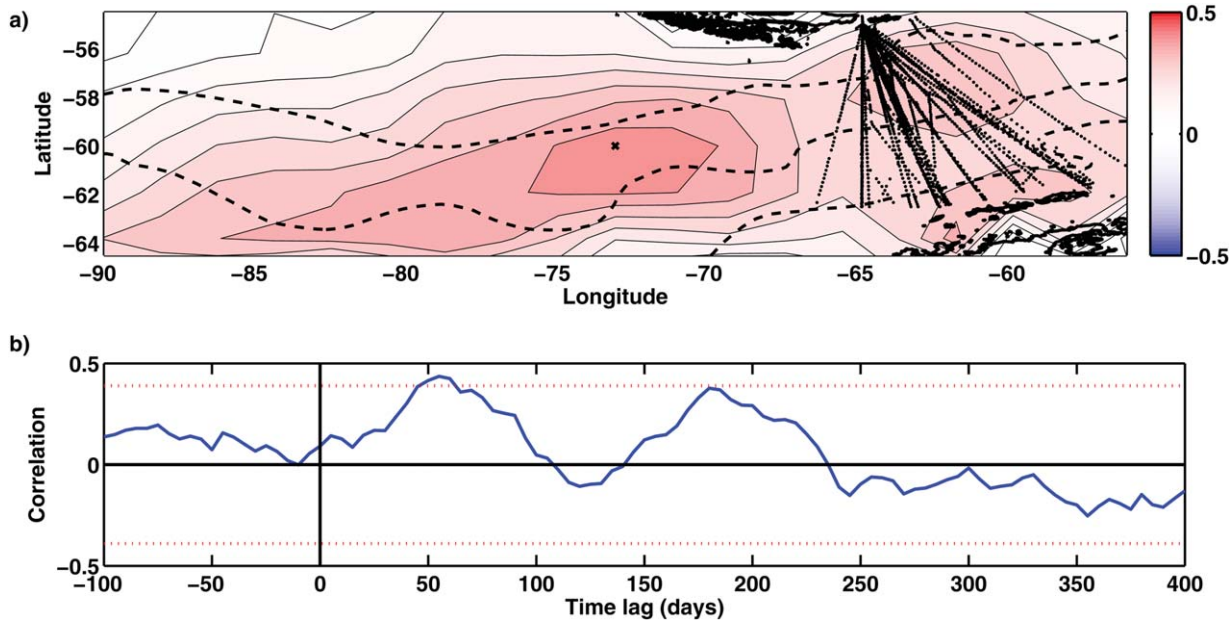

Figure 4. (a) Map of the correlation between $\mathcal{H}'_{400}$ and Q'_{net}55 days prior (Q_{55d}) shows a maximum near 60°S 73°W (black x). The interval between contours is 0.05. Climatologic position of the ACC fronts (dashed lines) are, from north to south, the Subantarctic Front, Polar Front, and southern ACC Front. Locations of XBT casts (black dots) are indicated. (b) The correlation between Q'_{net} at 60°S 73°W and $\mathcal{H}'_{400}$ reaches a maximum at ∼55 days. Positive time lag indicates that Q'_{net} precedes $\mathcal{H}'_{400}$. Confidence intervals ($p < .01$) are indicated by red dotted lines.

wind anomalies upstream of Drake Passage. We also examine the response of $\mathcal{H}'_{400}$ to large-scale patterns of climate variability associated with the ENSO and SAM indices.

[22] By vertically integrating an equation for the rate of change of upper-ocean temperature (equation (3) from *Qiu and Kelly* [1993]), we arrive at an expression relating

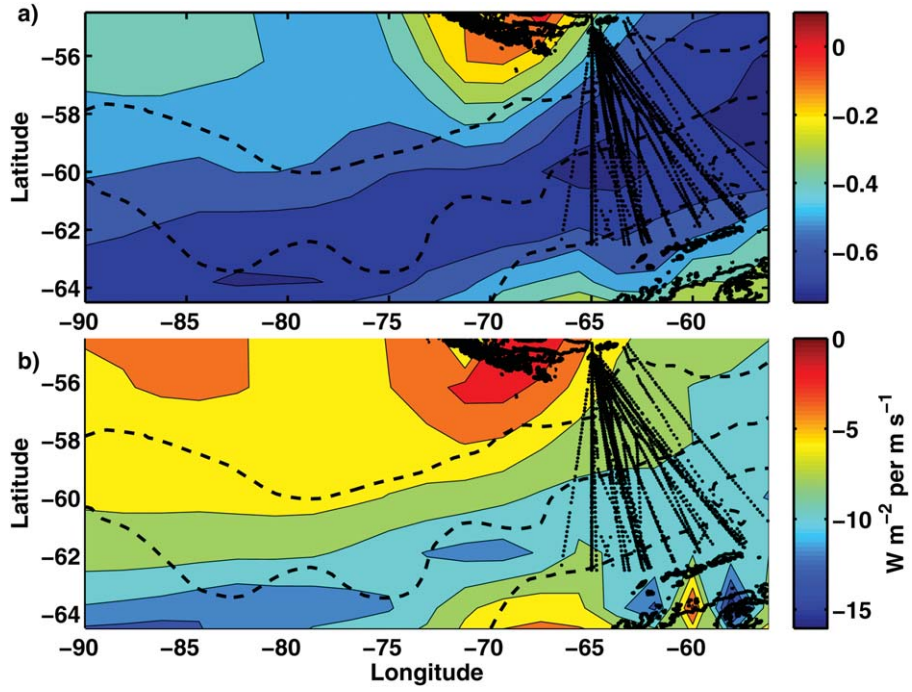

Figure 5. (a) Correlation of NCEP Reanalysis 2 heat flux anomalies (Q'_{net}) with meridional wind anomalies. (b) Regression coefficients of Q'_{net} onto meridional wind anomalies. Climatological positions of the ACC fronts (dashed lines) are, from north to south, the Subantarctic Front, Polar Front, and southern ACC Front. Locations of XBT casts (black dots) are indicated.

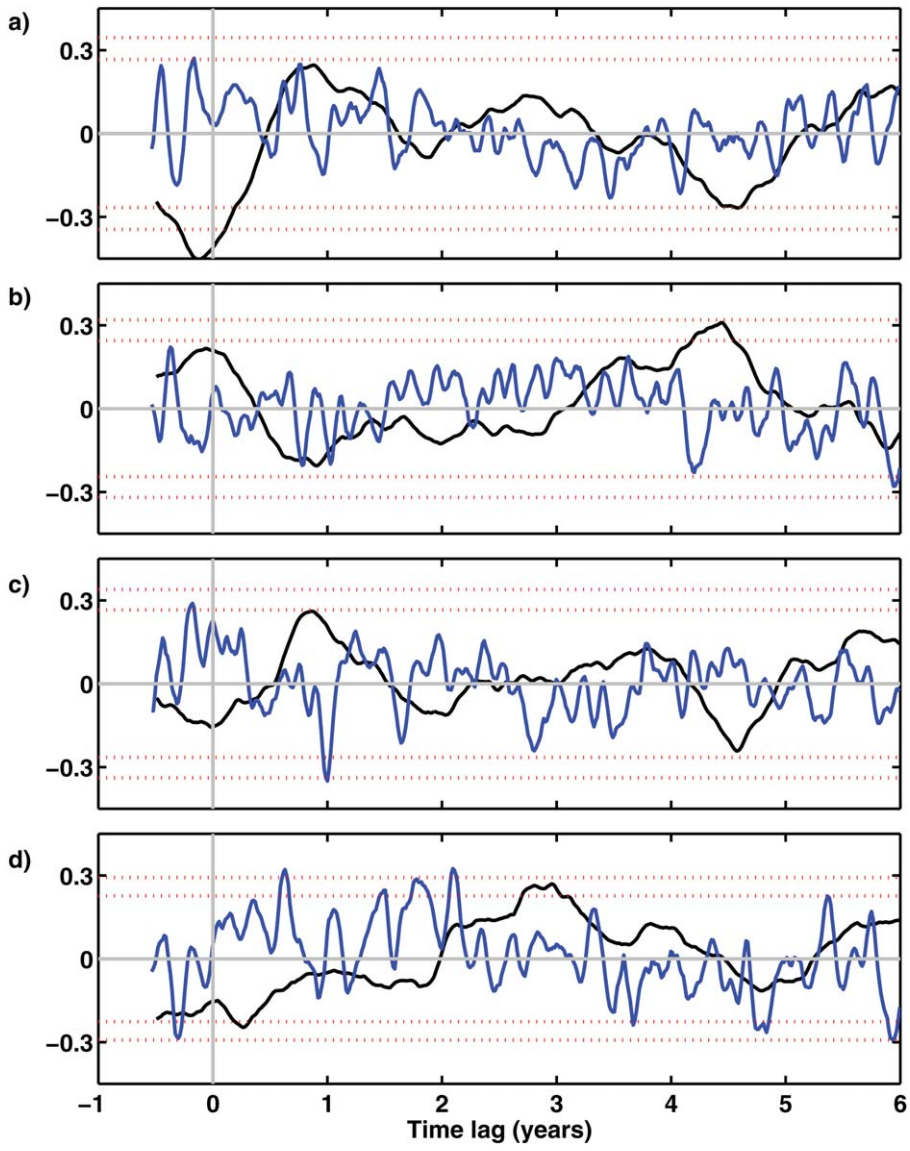

Figure 6. Correlations between the ENSO index (black line) or the SAM index (blue line) and (a) $\mathcal{H}_{400}$, (b)ϕ_{PF}, (c) $\mathcal{H}_N'$, and (d) $\mathcal{H}_S'$. Positive time lags indicate that the ENSO or SAM index precedes the XBT transect. Red dotted lines indicate the 0.95 and 0.99 significance levels.

upper-ocean heat content ($h_{400}(x,y)$) to surface heat fluxes ($Q)_{net}$, horizontal advection ($\overline{U}\cdot\nabla h_{400}(x,y)$), horizontal diffusion ($A_h\nabla^2 h_{400}(x,y)$) with a horizontal eddy viscosity A_h, and vertical entrainment ($\Delta T\nabla\cdot\overline{U}$):

$$\frac{\partial h_{400}(x,y)}{\partial t} = Q_{net} - \overline{U}\cdot\nabla h_{400}(x,y) + A_h\nabla^2 h_{400}(x,y) - \rho_0 c_p \Delta T\left(\nabla\cdot\overline{U}\right), \quad (3)$$

where $\overline{U}$ is the average current velocity of the upper 400 m and ΔT is a typical vertical temperature change across 400 m depth. In our approach to this study, we will directly examine a balance only between the heat content tendency averaged over the whole Drake Passage transect $\mathcal{H}_{400}$ and Q_{net}. The effects of advection on the upper-ocean heat balance can not be ignored, because heat content anomalies introduced upstream in the ACC can be advected into Drake Passage. We consider two advective processes: advected upper-ocean heat content anomalies may take the form of mesoscale eddies, which we examine in section 5, or result from anomalous surface buoyancy forcing warming or cooling a patch of water that is then advected by the mean flow of the ACC. In this section, we focus specifically on the sensitivity of Drake Passage heat content to anomalous air-sea fluxes in the ACC. We neglect vertical entrainment. We note that at 400 m depth (the base of the layer we are considering) temperature gradients are generally small, but it is possible that vertical mixing within the water column distributes surface heat flux input to depths greater than 400 m, potentially weakening the relationship between Q_{net}' and $\mathcal{H}_{400}'$ [*Stephenson et al.*, 2012]. Therefore, this calculation requires careful consideration of the horizontal, vertical, and temporal scales over which a signal is likely to persist.

[23] To determine where heat flux anomalies contribute most to heat content in Drake Passage, we constructed a map of the correlation between $\mathcal{H}'_{400}$ and Q'_{net} at points in and upstream of Drake Passage over a range of time offsets. The maximum correlation was found for Q'_{net} at 60°S 73°W at a time offset of 55 days (i.e., heat flux anomalies 55 days before a transect, Q_{55d}; $r = 0.44$; Figure 4a). In fact, at this location, lagged correlations of Q'_{net} with $\mathcal{H}'_{400}$ have significant positive correlations spanning a range of time offsets from 40 to 75 days (Figure 4b). At these time offsets, significant positive correlations with $r > 0.4$ cover a large area upstream (from ~58–64°S 68–82°W) of Drake Passage (Figure 4a). Thus the overall correlation pattern is consistent with downstream advection and is not overly sensitive to the time offset (Figure 4b) or location (Figure 4a). The regression coefficient between heat fluxes at 60°S 73°W and $\mathcal{H}'_{400}$ is $11.2 \pm 6.4 \times 10^{-3}\,\mathrm{GJ\,W^{-1}}$ (with 99% confidence interval). Typical heat flux anomalies, with Q'_{net} close to $\mathrm{O}(20\mathrm{Wm^{-2}})$, would lead to heat content anomalies of $\mathrm{O}(0.22\,\mathrm{GJ\,m^{-2}})$ with the use of this regression coefficient.

[24] Heat flux anomalies are negatively correlated with meridional wind anomalies, with stronger correlations centered over the Polar Front ($r \sim -0.7$; Figure 5a). Air temperature generally decreases poleward, so positive (northward) meridional wind anomalies tend to move cold air northward where it encounters warmer surface water, and negative (southward) wind anomalies tend to move warm air southward over cooler surface water. SST gradients are strong near the Polar Front, so winds that cross the front have the largest impact on air-sea heat flux. Regression coefficients of Q'_{net} onto meridional wind anomaly are also largest over the ACC, with magnitudes of 7.0 ± 0.4 to $10.0 \pm 0.5\mathrm{Wm^{-2}m/s}$ near the Polar Front (Figure 5b). A change of 0.5°C in air temperature would be sufficient to explain this regression coefficient; with an air temperature of 2°C, SST of 4°C, wind speeds of 1m/s and 80% relative humidity, a 0.5°C change in the air-sea temperature difference results in a change in sensible heat fluxes at the sea surface of $\sim 5\mathrm{Wm^{-2}}$ and a change in latent heat fluxes of $\sim 3\mathrm{Wm^{-2}}$. These estimates are consistent with turbulent heat fluxes observed from Drake Passage observations [*Jiang et al*., 2011].

[25] Meridional wind anomalies and heat flux anomalies are two mechanisms by which ENSO and SAM variability are imprinted on SST [e.g., *Meredith et al*., 2008; *Naveira Garabato et al*., 2009; *Ciasto and England*, 2011]. To observe the oceanic response to ENSO- and SAM-related forcing, we calculated lagged correlations of the ENSO and SAM indices with $\mathcal{H}'_{400}, \phi_{PF}, \mathcal{H}'_N$, and $\mathcal{H}'_S$ (Figure 6) at time offsets from −6 months to +6 years. To accommodate the irregular temporal sampling of the XBT transects, we linearly interpolated the monthly ENSO and SAM indices so as to keep the time offset from the date of the XBT transects constant for each correlation. Positive lags indicate that a transect occurs after the climate index. The time series of $\mathcal{H}'_{400}, \phi_{PF}, \mathcal{H}'_N$, and $\mathcal{H}'_S$ each have significant autocorrelation, which lowers the effective degrees of freedom (EDOF) in a correlation calculation and therefore the level at which correlations are significant. We interpolated each time series onto a monthly grid, computed the autocorrelation, and used as our decorrelation timescale twice the time it took for autocorrelation to decrease from 1 to 0.5. This led to decorrelation timescales of 3.5 months ($\mathcal{H}'_{400}$), (ϕ_{PF}), 3.2 months ($\mathcal{H}'_N$), and 2.5 months ($\mathcal{H}'_S$). Because the average temporal resolution of the XBT timeseries is 2 months, this leads to EDOF of 53 ($\mathcal{H}'_{400}$), (ϕ_{PF}), 58 ($\mathcal{H}'_N$), and 74 ($\mathcal{H}'_S$).

[26] The strongest correlations with ENSO occur when $\mathcal{H}'_{400}$ leads the ENSO index by 1–3 months ($r = -0.45$; Figure 6a). At this time lag, El Niño is associated with cooling of $\mathcal{H}'_{400}$ and $\mathcal{H}'_S$, as well as a northward shift of the Polar Front (Figure 6). Similarly, La Niña is associated with warming of $\mathcal{H}'_{400}$ and $\mathcal{H}'_S$ and a southward shift of the Polar Front (Figure 6). This relationship may be explained by anomalous heat flux input upstream of Drake Passage. At 60°S 71°W, Q'_{net} has its largest correlation with $\mathcal{H}'_{400}$. At this location, the strongest correlations between Q'_{net} and the ENSO index occur when Q'_{net} leads ENSO by 5–6 months ($r = -0.39$). If the resulting heat content anomalies require ~2 months (~55 days) to reach Drake Passage, we would expect a signal in $\mathcal{H}'_{400}$ that leads the ENSO index by 3–4 months. The timescale of this response shows good agreement with results from *Meredith et al*. [2008]; they found a negative response of SST near South Georgia Island, ~1500 km east of Drake Passage, at a lag of 5 months, but estimated that SST anomalies advected by the ACC would require 5–6 months to reach South Georgia Island from the western Antarctic Peninsula. We also find weak but significant correlations at time lags of 4.5 years (54 months), when ENSO and $\mathcal{H}'_{400}$ are negatively correlated ($r = -0.27$), ENSO and ϕ_{PF} are positively correlated ($r = 0.31$), and ENSO and $\mathcal{H}'_N$ are negatively correlated ($r = -0.24$). *Meredith et al*. [2008] found a negative correlation of South Georgia SST with ENSO at a lag of 60 months. So if the signal from ENSO is advected to South Georgia from Drake Passage in 5–6 months, a minimum in the correlation of Drake Passage heat content with ENSO would be expected at 54 months lag, which is consistent with what we observe.

[27] Compared with ENSO, the SAM shows more variability at monthly timescales, and lagged correlations of the SAM with upper-ocean heat content reflect this variability at short timescales. In general, heat content correlations with the SAM are weaker than those with ENSO. However, significant positive correlations are found between the SAM and $\mathcal{H}'_{400}$ when $\mathcal{H}'_{400}$ leads by 2 months ($r = 0.27$; Figure 6a). At this same time lag, warm anomalies in $\mathcal{H}'_{400}$ and $\mathcal{H}'_N$ (Figure 6c) are associated with a positive SAM and cold anomalies with a negative SAM. At short time offsets, other studies have found similar positive relationships between the SAM and SST [e.g., *Kwok and Comiso*, 2002; *Liu et al*., 2004] and between the SAM and temperatures at depths of 0–400 m north of the Polar Front [*Sprintall*, 2008]. The heat content responses may be linked to heat fluxes or meridional wind anomalies associated with the SAM.

[28] At 60°S 73°W, where $\mathcal{H}'_{400}$ and Q_{net} were significantly correlated at 55-day lag (Figure 4a), significant correlations were found between the SAM index and Q'_{net}, with Q'_{net} leading the SAM by 4 months ($r = 0.24$), and between the SAM index and meridional wind anomalies, with wind anomalies leading the SAM by 1–2 months ($r = -0.24$).

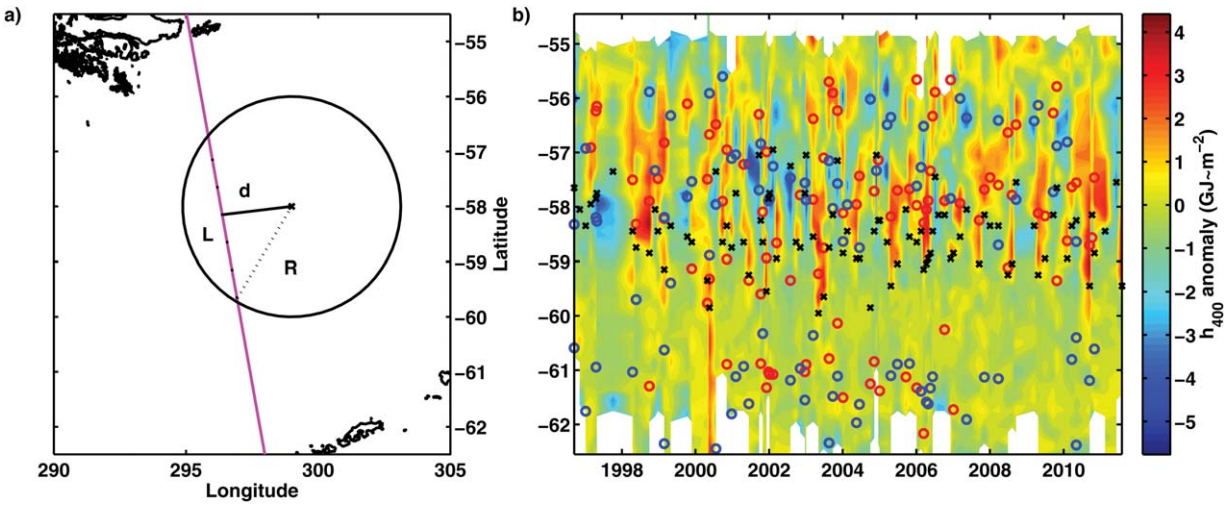

Figure 7. (a) Schematic depiction of determination of the heat content anomaly associated with a transect crossing an eddy (not to scale). The length, L, of the intersection between a transect (magenta line) and an eddy (black circle) depends on the minimum distance, d, from the center of the eddy to the transect and the length scale, R, of the eddy. (b) Upper-ocean heat content anomalies, h'_{400}, relative to a seasonal cycle and a spatial mean (binned by latitude). The latitude of cold-core (blue circles) and warm-core (red circles) eddies that intersect an XBT transect are indicated, as well as the location of the Polar Front (black x).

[29] South of the Polar Front, upper-ocean heat content is correlated with ENSO and the SAM on timescales different from those north of the Polar Front (Figure 6d). Correlations of $\mathcal{H}'_S$ with ENSO have a peak at a lag of ~3 years ($r = 0.27$), when correlations of ENSO with $\mathcal{H}'_{400}, \phi_{PF}$ and $\mathcal{H}'_N$ are not significant (Figure 6). Significant peaks in the correlations of the SAM with $\mathcal{H}'_S$ occur at lags of ~8 months ($r = 0.32$) and 24 months ($r = 0.32$). Several studies have illustrated the importance of interactions between atmospheric forcing, sea ice extent along the western Antarctic Peninsula, and resulting changes to the upper ocean during both ENSO and SAM events [e.g., *Yuan and Martinson*, 2000; *Meredith et al*., 2008; *Sprintall*, 2008; *Naveira Garabato et al*., 2009]. For example, sea ice extent around Antarctica has been strongly linked to advection or thermodynamic effects related to wind forcing [*Holland and Kwok*, 2012]. Sea-ice extent at 70°W, just west of Drake Passage, varies in phase with ENSO and in antiphase with the SAM, and it is negatively correlated with SST at South Georgia Island at a few months' lag [*Meredith et al*., 2008]. At longer timescales, sea ice extent near the western Antarctic Peninsula is positively correlated with ENSO at lags of 18–30 months [*Yuan and Martinson*, 2000], similar to the 3-year response of $\mathcal{H}'_S$. There is some debate over the response of the Southern Ocean to increased zonal wind stress associated with the SAM. In response to a positive SAM event, warm anomalies in $\mathcal{H}'_S$ may result from increased upwelling of warm upper CDW [*Hall and Visbeck*, 2002], or alternately may result from increased eddy activity and an increase in the poleward heat transport driven by eddies [*Hogg et al*., 2008]. A positive SAM index has been linked also to increased rates of sea ice growth in the Pacific sector at lags of 0 and 1 year [*Holland et al*., 2005]; interaction of sea ice with the upper ocean south of the Polar Front may explain the presence of two peaks roughly 1 year apart in the correlation of the SAM with $\mathcal{H}'_S$ (Figure 6d).

5. Variability Due to Eddies and Meanders

[30] As in other regions of the Southern Ocean, upper-ocean variability in Drake Passage is dominated by mesoscale eddies and meanders of the fronts of the ACC [*Sprintall*, 2003, 2008]. However, the degree to which the Southern Ocean is eddy saturated, and therefore the response of meridional heat transport in the ACC to changing ENSO and SAM, remains a subject of inquiry [e.g., *Böning et al*., 2008; *Hogg et al*., 2008]. The goal of this section is to quantify the heat content anomalies associated with mesoscale eddies and meanders of the Polar Front in Drake Passage. The analysis in section 3 aims to capture only the impact of frontal meanders, whereas the eddy database used in this section is designed to track eddy motions but also includes frontal meanders when they are indistinguishable from eddies. We first construct composite cold-core and warm-core eddies as identified in the tracked eddy database and sampled by the XBT transects; then we determine the mesoscale anomalies in heat content associated with an eddy or meander. Finally, we calculate the contribution of eddies and meanders to variability in $\mathcal{H}'_{400}$.

[31] To identify mesoscale features associated with eddies and meanders, we classify a transect as crossing or intersecting an eddy when the distance from the eddy center to a point in the transect (d, as illustrated in Figure 7a) is less than the length scale (R, as shown in Figure 7a) associated with the eddy in the *Chelton et al*. [2011b] database. Most of the XBT transects crossed at least one eddy (Figures 2 and 7b), with a total of 95 warm-core and 90 cold-core eddies sampled. Two distinct bands of eddy activity are noted: one band located between 56°S and 59.5°S,

Table 2. Mean Properties of Eddies From *Chelton et al.*'s [2011b] Database Intersected by a Drake Passage XBT Transect: The Number of Each Type of Eddy (N), the Average Amplitude (A), Effective Length Scale (R), and Latitude[a]

	Total	N of PF	S of PF
Warm core			
N	95	57	38
A (cm)	14.4 ± 1.0	18.2 ± 1.2	8.6 ± 1.1
R (km)	79.3 ± 2.3	84.6 ± 2.7	71.3 ± 3.8
Lat. (°S)	58.4 ± 0.2	57.2 ± 0.1	60.0 ± 0.2
Cold core			
N	90	18	72
A (cm)	-13.1 ± 0.9	-15.8 ± 1.7	-12.4 ± 1.1
R (km)	75.7 ± 2.6	73.4 ± 4.0	76.3 ± 3.0
Lat. (°S)	59.1 ± 0.2	56.7 ± 0.2	59.7 ± 0.2

[a]Averages are computed over all warm- or cold-core eddies, or over eddies north or south of the Polar Front, and ±1 standard error is reported for all quantities.

probably associated with the Polar Front, and another cluster near 61°S, possibly associated with the Southern Antarctic Circumpolar Current Front (Figure 7b). The largest, most intense eddies occur near to or north of the Polar Front, whereas eddies south of the Polar Front are smaller and have lower amplitude (Figure 2; Table 2). These results agree with measurements in Drake Passage that show greater eddy kinetic energy (EKE) north of the Polar Front than south [*Lenn et al.*, 2007].

[32] The net effects of warm-core or cold-core eddies on upper-ocean heat content were evaluated by averaging values of $\mathcal{H}'_{400}, \mathcal{H}'_N, \mathcal{H}'_S$ over transects that intersected (1) any warm-core eddies, (2) any cold-core eddies, (3) warm-core eddies north of the Polar Front, (4) warm-core eddies south of the Polar Front, (5) cold-core eddies north of the Polar Front, or (6) cold-core eddies south of the Polar Front (Table 3). There is some overlap between the set of transects used to compute averages in each column. For example, transects that intersected both warm-core and cold-core eddies contribute to the averages in the warm-core total and cold-core total columns in Table 3. On average, transects that intersected any warm-core eddy showed a slight increase in $\mathcal{H}'_N$. Transects that intersected warm-core eddies north of the Polar Front exhibit significant increases in $\mathcal{H}'_{400}$, a southward displacement of the Polar Front, and an increase in $\mathcal{H}'_N$ (Table 3). In contrast, transects that intersected a warm-core eddy south of the Polar Front were associated with cool anomalies in $\mathcal{H}'_{400}$ and $\mathcal{H}'_N$ but did not show significant differences in $\mathcal{H}'_S$ or $\Delta\phi_{PF}$ (Table 3). The difference in response may reflect differences in the number, size, and types of eddies intersected north as opposed to south of the Polar Front. Warm-core eddies south of the Polar Front are fewer, smaller, and lower in amplitude than warm-core eddies north of the Polar Front (Table 2). The presence of cold-core or warm-core eddies north of the Polar Front results in a southward shift in ϕ_{PF} (Table 3). Conversely, transects in which cold-core eddies are intersected south of the Polar Front show overall cooling of $\mathcal{H}'_{400}$ and a northward shift in ϕ_{PF}.

[33] Although we can not explicitly distinguish between eddies and meanders in our identification criteria, we expect that they will have different effects on $\mathcal{H}'_N$ and $\mathcal{H}'_S$. Southward (warm) meanders of the Polar Front may be included in our analysis as warm-core eddies located north of the Polar Front, whereas northward (cold) meanders of the Polar Front may be classed with cold-core eddies located south of the Polar Front. In section 3, we showed that although meanders of the Polar Front are strongly linked to changes in $\mathcal{H}'_{400}$, they are not significantly correlated with changes in $\mathcal{H}'_N$ or $\mathcal{H}'_S$ (Table 1). Similar results are presented in Table 3; significant changes in $\mathcal{H}'_{400}$ are evident in the averages that include potential meanders (warm-core north of the Polar Front or cold-core south of the Polar Front), whereas transects that include cold-core eddies north of the Polar Front show a large decrease in $\mathcal{H}'_N$ but do not have a significant effect on $\mathcal{H}'_{400}$ (Table 3).

[34] To examine the mesoscale variability in upper-ocean heat content associated with eddies, we calculated the spatially varying heat content, h_{400} (equation (1)), and formed anomalies relative to a meridionally varying mean constructed by averaging at each 0.1° latitude point over all 93 objectively mapped temperature transects. Then, for points located north of the Polar Front, the seasonal cycle corresponding to $\mathcal{H}_N$ was removed; for points south of the Polar Front, the seasonal cycle in $\mathcal{H}_S$ was removed. The resulting field of spatially varying upper-ocean heat content anomalies (henceforth h'_{400}) therefore differs from the regional averages discussed in sections 3 and 4. Indeed, h'_{400} shows considerable mesoscale activity, with strong anomalies near the latitude of the Polar Front (Figure 7b).

[35] The spatial structure of heat content anomalies h'_{400} associated with typical eddies is examined by the construction of composite eddies. To make composite cold-core and warm-core eddies, we calculated zonal and meridional displacement of XBT casts from the centers of nearby eddies, with distances normalized by the length scale of the eddy, R. In total, ~200 measurements of h'_{400} were collected within one eddy length scale of the center of an eddy. Heat content anomalies were binned by distance (bin sizes of 0.5 R) and direction (60° bins) from the center of

Table 3. Averages of $\mathcal{H}'_{400}, \mathcal{H}'_N$, and $\mathcal{H}'_S$ for All Transects That Intersected Warm-Core or Cold-Core Eddies and for Transects That Intersected Warm-Core or Cold-Core Eddies North or South of the Polar Front[a]

	All	N of PF	S of PF
Warm core			
N	74	60	26
$\mathcal{H}'_{400}$(GJ m^{-2})	0.06 ± 0.06	0.15 ± 0.06[b]	-0.17 ± 0.09[b]
$\mathcal{H}'_N$(GJ m^{-2})	0.14 ± 0.07[b]	0.23 ± 0.08[b]	-0.13 ± 0.11[b]
$\mathcal{H}'_S$(GJ m^{-2})	0.00 ± 0.04	-0.00 ± 0.05	0.04 ± 0.06
$\Delta\phi_{PF}$(km)	-8 ± 9	-18 ± 9[b]	14 ± 17
Cold core			
N	65	34	45
$\mathcal{H}'_{400}$(GJ m^{-2})	-0.06 ± 0.06	-0.08 ± 0.08	-0.10 ± 0.08[b]
$\mathcal{H}'_N$(GJ m^{-2})	0.00 ± 0.08	-0.24 ± 0.11[b]	0.10 ± 0.10
$\mathcal{H}'_S$(GJ m^{-2})	0.02 ± 0.05	0.12 ± 0.08[b]	-0.04 ± 0.05
$\Delta\phi_{PF}$(km)	5 ± 9	-20 ± 10[b]	20 ± 11[b]

[a]The displacement of the Polar Front ($\Delta\phi_{PF}$) is computed relative to the mean latitude of the Polar Front (58.5°S) over the 93 XBT transects. Error bounds are 1 standard error.
[b]Significant at 1 standard error.

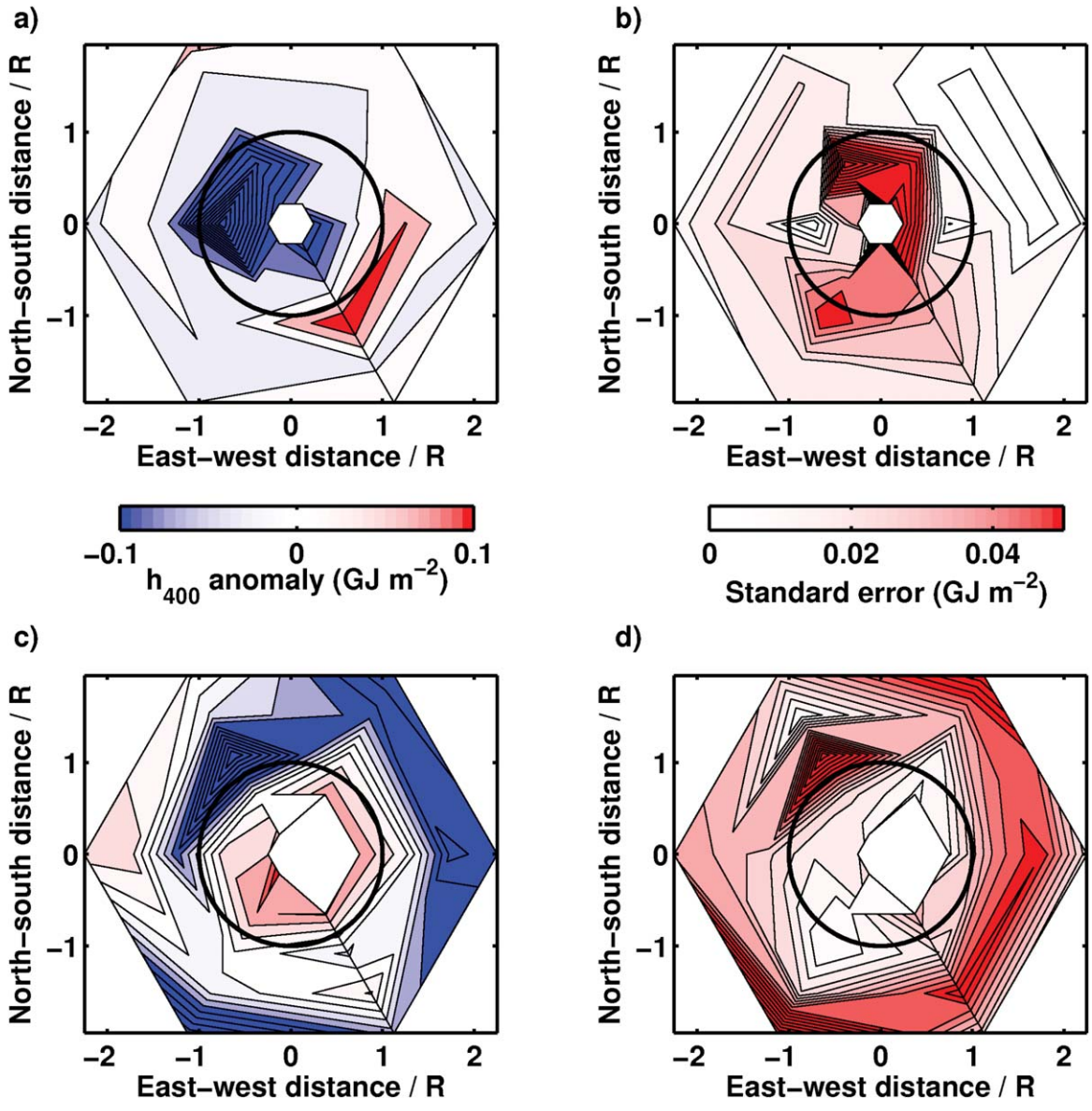

Figure 8. Spatial distribution of h'_{400} in (a) a composite cylonic (cold-core) eddy and (c) a composite anticyclonic (warm-core) eddy. For heat content measurements near an eddy, values of h'_{400} were normalized by the eddy's amplitude (units are GJ m^{-2}per cm eddy amplitude) and binned by position relative to the eddy center. Zonal and meridional displacement from the center of the eddy is scaled by the effective length scale of the eddy. The standard error of the bin average is shown for (b) the cyclonic eddy and (d) the anticyclonic eddy. Contour intervals are 0.05 (Figures 8a and 8c) or 0.01 (Figures 8b and 8d) GJ m^{-2} per cm.

the eddy to the measurement location, with cold-core and warm-core eddies considered separately (Figure 8). The resulting composites show that the eddy length scale is an appropriate scaling to describe heat content variations associated with mesoscale eddies; the cold or warm anomaly is nearly contained (78% and 86%, respectively) within a circle of radius equal to the eddy length scale (Figure 8).

[36] Eddies appear to be rotationally and east-west asymmetric. In the composite cold-core eddy, a cold anomaly of -0.29 ± 0.10 GJ m^{-2}per cm eddy amplitude is concentrated on the west side of the composite eddy, but a warm anomaly is found along the eddy's eastern edge (Figure 8a). The warm-core composite eddy has a smaller peak temperature anomaly, 0.14 ± 0.03 GJ m^{-2}per cm and has a cold anomaly along its western edge (Figure 8c). The appearance of these composite eddies is likely dominated by the large-amplitude eddies near the Polar Front and influenced by the prevailing SW-NE orientation of the Polar Front in Drake Passage (Figure 1). The counterclockwise spiral of the cool temperatures at the edge of the warm-core eddy is consistent with anticyclonic movement (in the Southern Hemisphere) of water across a SW-NE–oriented front (Figure 8c). The warm anomaly along the edge of the cold-core eddy (and similarly the cold anomaly at the edge of the warm-core eddy) gives the composite eddy a dipole structure. Although the standard error in the

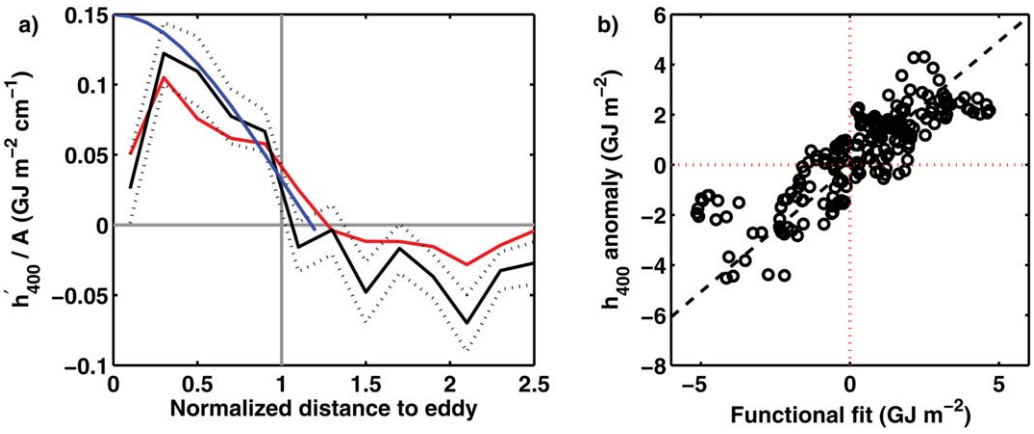

Figure 9. (a) The heat content anomaly (h'_{400}) associated with the eddy is a function of distance from the eddy center, d, and the length scale, R, and amplitude, A, of the eddy. For measurements located within an eddy, h'_{400} was normalized by the amplitude of the eddy; binned averages of h'_{400}/A were computed at d/R ranging from 0.1 to 2.5. Mean (black line) ± 1 standard error (dotted lines) and median (red) h'_{400}/A decrease from maxima near 0.3 R from the eddy center to 0 at 1–1.3 R from the center. A truncated Gaussian curve (blue line) as in equation (3) approximates $f(r,A)$. (b) A scatterplot of h'_{400} against the value of $f(r,A)$ at each measurement point (black circles) and the one-to-one line fit (dashed line).

mean heat content anomaly is large for some bins, portions of the dipole shape appear to be significant at two standard errors in both the cold-core and warm-core eddies (Figures 8b and 8d, respectively). *Chelton et al*. [2011a] noted a similar asymmetric structure in ocean color maps of composite eddies and suggested that it might result from advection due to cyclonic rotation around the cold eddy core (clockwise in the Southern Hemisphere) or anticyclonic advection around a warm eddy core, or that the dipole might indicate local upwelling induced by eddy pumping.

[37] To estimate the net contribution of eddies to upper-ocean heat content, we consider a simplified model of a rotationally symmetric eddy where h_{400} is a function, $f(r,A)$, of the distance from the eddy center, r, and the eddy amplitude, A. We normalized h'_{400} by the (signed) amplitude, A, of the eddy and normalized distance from the eddy center by the length scale of the eddy, R. The mean and median values of h'_{400}/A were computed over bins of width 0.2 R (Figure 9a). The mean normalized heat content anomaly decreases from a peak of $0.12 \pm 0.02\,\mathrm{GJ\,m^{-2}}$ in the interior of an eddy to $0.03 \pm 0.02\,\mathrm{GJ\,m^{-2}}$ at a distance equal to the eddy length scale. The median heat content anomaly crosses zero at a distance of $\sim 1.3 \times R$ from the eddy center. We approximate these curves by a truncated Gaussian curve given by the expression

$$f(r,A) = 0.15A\left(2e^{-r^2/2R^2} - 1\right) \tag{4}$$

over distances $|r| < 1.2R$ and zero outside this range (Figure 9a). Because the eddy length scale is defined by the area bounded by the maximum azimuthally averaged velocity (see section 2.2) a strong gradient is appropriate at a distance $r = R$ from the eddy center. A coefficient of 0.15 ± 0.02 (99% confidence interval) comes from a linear regression of h'_{400}/A onto $f(r,A)$ (Figure 9b). There is good agreement between the functional fit and observed values of h'_{400} ($r = 0.82$; Figure 9b), and results are not critically dependent on the functional form of $f(r,A)$. For example, assuming a cylindric eddy with constant amplitude A where $r < R$ also gives a good correlation (correlation coefficient = 0.77, not shown).

[38] How realistic are these coefficients relating heat content to eddy amplitude? Thermosteric expansion of seawater contributes significantly to sea surface height variability. For typical conditions in Drake Passage (salinity ~34 psu, temperature ranging from −1°C to 8°C), the thermal expansion coefficient $\alpha \approx 5 - 10 \times 10^{-5}\,^{\circ}\mathrm{C}^{-1}$. A warming of 1°C over a water column 400 m deep is equivalent to an increase of $1.6\,\mathrm{GJ\,m^{-2}}$ of heat over a sea surface height increase of ~2–4 cm; equivalent to $h'_{400}/A \approx 0.4 - 0.8\,\mathrm{GJ\,m^{-2}}$ per cm sea surface height anomaly. The peak value of the functional fit in equation (3) relating heat content anomaly to eddy amplitude is $0.15 \pm 0.02\,\mathrm{GJ\,m^{-2}}$ per cm, ~20 to 40% of the value expected to be due to thermal expansion. The difference can be explained if eddies extend over the upper 1000–2000 m of the water column; this is not implausible because some Southern Ocean eddies have been classed as "equivalent barotropic" [e.g., *Firing et al*., 2011]. We performed similar regression fits to equation (3) for heat content anomalies calculated over a range of depths (not shown), and results suggest that the vertical variations of heat content anomalies within an eddy may have an approximate e-folding scale between 520 and 830 m.

[39] Based on the functional fit in equation (4), a typical warm-core eddy near 57°S with amplitude 18.2 ± 1.2 cm and length scale 84.6 ± 2.7 km (Table 2) represents a total area-integrated heat anomaly of $22.9 \pm 3.1 \times 10^{18}$J in the upper 600 m; a typical eddy near 60°S, with amplitude 8.6 ± 1.1 cm and length scale 71.3 ± 3.8 km, represents an anomaly of only $7.7 \pm 1.5 \times 10^{18}$J. The contribution of any single eddy to the transect-averaged heat content anomaly, $\mathcal{H}'_{400}$, is a function not only of the eddy's amplitude and

length scale, but also of the length of the overlap of the transect with the eddy which, in turn, is prescribed by the proximity of the eddy to the transect and the length scale of the eddy. A schematic depicting this relationship is shown in Figure 7a. For a circular eddy, the length of the overlap, L, of the transect and the eddy can be expressed as

$$L = 2 \times \sqrt{R^2 - d^2}, \tag{5}$$

where R is the length-scale of the eddy, and d is the minimum distance from the eddy to the transect.

[40] The total heat content anomaly associated with sampling a single eddy, h_e, can be expressed as an integral along the portion of the transect that lies within a distance R of the eddy's center (Figure 7a):

$$h_e = \int_{-\sqrt{R^2-d^2}}^{\sqrt{R^2-d^2}} f\left(\sqrt{d^2 + l^2}, A\right) dl, \tag{6}$$

where the integration variable l ranges from $+L/2$ to $-L/2$ (as in equation (5)). The total heat content anomaly due to eddies and meanders in a transect, $\mathcal{E}$, is the sum of h_e (equation (6)) along segments where a transect intersects individual eddies divided by the length of the transect. A regression of $\mathcal{E}$ onto $\mathcal{H}'_{400}$ (Figure 10) shows that the amplitude of heat content anomalies due to eddies and meanders closely matches the amplitude of the observed heat content anomalies. Variations in $\mathcal{E}$ are also well correlated with $\mathcal{H}'_{400}$ ($r = 0.604$; Table 1). The effects of uncertainty in the amplitude of $f(r,A)$ on h_e were modeled as a fixed percentage of the total of $\pm 13\%$ of h_e, based on the uncertainty in the amplitude of the function $f(r, A)$ of $\pm 0.02\,\mathrm{GJ\,m^{-2}}$ per cm relative to a value of $0.15\,\mathrm{GJ\,m^{-2}}$ per cm at $r = 0$. We also estimated the sensitivity of h_e to a $\pm$ 10 km change in d for R ranging from 20 to 90 km and d ranging from 0 to R; this represents uncertainty in the location of the center of the eddy. Averaged over the ~850 km length of a typical transect, uncertainty in the eddy position contributes an additional uncertainty in $\mathcal{E}$ of less than $4 \times 10^{-3}\,\mathrm{GJ\,m^{-2}}$ per eddy.

6. Significant Contributors to Heat Content

[41] This study has explored contributors to interannual variability in upper-ocean heat content in Drake Passage. In sections 3–5, we identified variables that have significant relationships with $\mathcal{H}'_{400}$: the Polar Front latitude as determined from XBT transects (ϕ_{PF}; section 3), heat flux anomalies (Q'_{55d}; section 4), the ENSO index at −45 day lag and the SAM index at −60 day lag (section 4), and heat content anomalies associated with mesoscale eddies and frontal meanders ($\mathcal{E}$; section 5). In this section, we rank these terms in importance.

[42] A first approach to ranking terms in importance is the calculation of linear correlation coefficients of each variable individually with $\mathcal{H}'_{400}$. By this measure, the single best predictor of $\mathcal{H}'_{400}$ is $\mathcal{E}$ ($r = 0.60$), followed by ϕ_{PF} ($r = 0.55$), ENSO ($r = -0.45$), Q_{55d} ($r = 0.44$), and SAM ($r = 0.27$). However, these variables are not entirely independent from each other. For example, heat flux anomalies have been linked to both ENSO and the SAM, and the SAM and ENSO are correlated with each other. Furthermore, a change in the location of the Polar Front may be represented in both ϕ_{PF} and $\mathcal{E}$ because frontal meanders may appear in the tracked eddy database. To get an understanding of the independent contributions of each variable to $\mathcal{H}'_{400}$, we use the technique of partial correlations, also known as residualization. This allows us to examine statistical relationships between, for example, ϕ_{PF} and $\mathcal{H}'_{400}$ while controlling for variations in ENSO, the SAM, Q_{55d}, and $\mathcal{E}$. To perform this calculation, we make a linear regression of ϕ_{PF} onto the four variables for which we are controlling (in this case, ENSO, the SAM, Q_{55d}, and $\mathcal{E}$) and compute the residual. The correlation of the residual with $\mathcal{H}'_{400}$ is the semipartial correlation; the square of this semipartial correlation gives the fraction of variance of $\mathcal{H}'_{400}$ attributable to ϕ_{PF} alone.

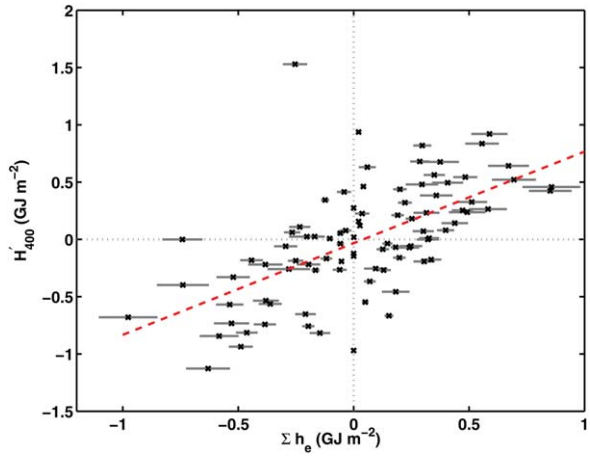

Figure 10. Scatterplot of $\mathcal{H}'_{400}$ against the sum of heat content anomalies due to eddies ($\mathcal{E}$). A linear regression (red dashed line) has a slope of 0.80 ± 0.22. Uncertainties in $\mathcal{E}$ (gray lines) are computed as discussed in section 5.

[43] The semipartial correlations effectively rank the terms in order of which adds the most information to a linear model of $\mathcal{H}'_{400}$. With this method, the variable that independently contributes the most to variance in $\mathcal{H}'_{400}$ is $\mathcal{E}$ ($r = 0.34$; controlling for ϕ_{PF}, ENSO, SAM, and Q_{55d}). The second most important term is ENSO ($r = -0.28$, controlling for $\mathcal{E}, \phi_{PF}$, SAM, and Q_{55d}). Only these first two variables ($\mathcal{E}$ and ENSO) show formally statistically significant semipartial correlations with $\mathcal{H}'_{400}$; the other variables are sufficiently cross-correlated with each other that isolating their effects reduces the semipartial correlations below significant levels. The remaining semipartial correlations, in descending order, belong to ϕ_{PF} ($r = -0.20$; controlling for $\mathcal{E}$, ENSO, SAM, and Q_{55d}), Q_{55d} ($r = 0.18$; controlling for $\mathcal{E}, \phi_{PF}$, ENSO, SAM), and the SAM index at −60 day lag ($r = 0.08$; controlling for $\mathcal{E}, \phi_{PF}$, ENSO, and Q_{55d}). We note that the semipartial correlation of ϕ_{PF} with $\mathcal{H}'_{400}$ is much smaller than the simple correlation; $\mathcal{E}$ and ϕ_{PF} are strongly correlated with each other, as both register changes in the location of the Polar Front.

[44] For this study, the value of the semipartial correlations lies in their use for ranking the importance of variables as predictors of upper-ocean heat content anomalies in Drake Passage. If we reconstruct $\mathcal{H}'_{400}$ with a multiple

linear regression of $\mathcal{H}'_{400}$ onto $\mathcal{E}$ and ENSO, the linear regression is strongly correlated with $\mathcal{H}'_{400}(r = 0.73)$. Adding the next two terms, ϕ_{PF} and Q_{55d}, only slightly improves a reconstruction of $\mathcal{H}'_{400}$ by multiple linear regression of $\mathcal{H}'_{400}$ onto $\mathcal{E}$, ENSO, ϕ_{PF}, and $Q_{55d}(r = 0.78)$; in other words, a linear combination of those four terms accounts for 61% of the variance in $\mathcal{H}'_{400}$. Explicitly including the SAM index in the regression does not appreciably increase the fraction of variance explained; however, we note that the effects of SAM on $\mathcal{H}'_{400}$ are not independent from those of ENSO, heat fluxes, and Polar Front meanders. Finally, if we consider upper-ocean heat content variability at all timescales, as represented by $\mathcal{H}'_{400}$, we find that the weighted sum of five terms ($\mathcal{E}$, ϕ_{PF}, the ENSO index at -45 day lag, Q_{55d}, and the seasonal cycle in $\mathcal{H}_{400}$ computed in section 3) is correlated at $r = 0.91$ with $\mathcal{H}_{400}$.

7. Summary and Conclusions

[45] A 16 year record of XBT temperature transects was used to examine intraseasonal and interannual variations in upper-ocean heat content in Drake Passage. The oceanic variability present in the form of mesoscale eddies and the response to climate forcing was found to be different for regions north and south of the Polar Front. Perhaps as a result, changes in heat content north of the Polar Front and shifts in the location of the Polar Front contribute more to interannual variability in the amount of heat above 400 m depth in Drake Passage than do changes in heat content south of the Polar Front.

[46] On the >2 month timescales that we examined, anomalous heat fluxes are a significant source of variability in upper-ocean heat content. In particular, we found a maximum in correlation between $\mathcal{H}'_{400}$ and heat flux anomalies ~250 km west of Drake Passage ~2 months prior to a transect. Heat flux anomalies appear to be closely related to meridional wind anomalies in the Southern Ocean, as others studies have also noted [e.g., *Kwok and Comiso*, 2002; *Meredith et al*., 2008; *Naveira Garabato et al*., 2009]. Atmospheric teleconnections to ENSO and large-scale forcing related to the state of the SAM affect both heat fluxes and wind anomalies, with the result that ENSO and SAM are correlated with heat content at several time offsets. Our results are broadly consistent with other studies that have looked at the effects of ENSO and SAM on Southern Ocean temperatures [*Kwok and Comiso*, 2002; *Liu et al*., 2004; *Meredith et al*., 2008; *Sprintall*, 2008; *Naveira Garabato et al*., 2009], although the time lags differ in some cases from these other results. Qualitative differences in ocean forcing associated with individual ENSO events included or excluded from these studies that cover different time periods may explain the range of temporal response scales observed. We find significant correlations between ENSO and $\mathcal{H}'_{400}$ at lags of -1 to -2 months, as well as 4.5 years; weak but statistically significant correlations are found between the SAM and $\mathcal{H}_{400}$ at a time lag -2 months. Important differences are seen in the response to ENSO and SAM of upper-ocean heat content south of the Polar Front. $\mathcal{H}'_S$ responds to ENSO at ~0 and 3 year lags and responds to the SAM at 8 month and 24 month lags. Although the mechanisms responsible for the difference in response north and south of the Polar Front are not clear, interactions of the atmosphere and ocean with sea ice may contribute to the observed regional variation [*Yuan and Martinson*, 2000; *Holland et al*., 2005].

[47] Meanders and eddies have been suggested as the dominant source of upper-ocean variability in Drake Passage [*Sprintall*, 2003, 2008]. Our results support these claims. Sources of mesoscale variability in the form of eddies or meanders were identified with the use of *Chelton et al*.'s [2011b] tracked eddy database. In 90 transects for which a tracked eddy database was available, 95 warm-core and 90 cold-core eddies were sampled by XBTs and composite cold-core and warm-core eddies were constructed. The composite pictures of the heat content anomaly of an eddy show a number of well known features of eddies: rotational and east-west asymmetry, and warm or cold heat content anomalies near the edge of the eddy with an opposite sense to that of the eddy which is likely associated with upwelling or advection [*Chelton et al*., 2011a]. A fit was made to the heat content in an eddy as a function of distance from the center; variations in the coefficient associated with this fit suggest that temperature anomalies within a composite eddy may be "equivalent barotropic." Based on the functional fit and eddy characteristics from *Chelton et al*.'s [2011b] database, the contribution of eddies and meanders to upper-ocean heat content was estimated to be more than one third of the interannual variability.

[48] In total, heat fluxes (seasonal and interannual), meanders, eddies, and ENSO variability explain ~84% of the variance of heat content in Drake Passage at all timescales, with the largest contributions coming from the seasonal cycle in surface heat fluxes, variability associated with mesoscale eddies and frontal meanders, and ENSO teleconnections. ENSO teleconnections have a significant effect on upper-ocean heat content, but the response may be only partially explained by ENSO-driven modifications to the surface heat fluxes and meridional wind field. This study did not fully explore the link between large-scale atmospheric forcing and mesoscale ocean features. Strengthening winds over the Southern Ocean are associated with increases in eddy kinetic energy in the ACC [*Meredith and Hogg*, 2006]; an enhanced eddy field may simply lead to greater variability in upper-ocean heat content or it may lead to enhanced poleward heat transport, setting the stage for ocean warming south of the Polar Front.

[49] **Acknowledgments.** Data collection and analysis for this project was funded by NSF grants to S.T.G. (ARRA OCE08050350) and J.S. (ANT0943818) and a NASA grant to S.T.G. (NNX08AI82G). G.R.S. acknowledges a NASA Earth and Space Science Fellowship and the ARCS Foundation for their support. S.T.G. acknowledges sabbatical support from the French Centre National de la Recherche Scientifique and Observatoire Midi-Pyrénées. NCEP Reanalysis 2 data were provided by the NOAA/OAR/ESRL PSD, Boulder, Colorado, USA, from their web site at http://www.esrl.noaa.gov/psd. ECMWF-Interim Reanalysis data were provided by the European Centre for Medium-Range Weather Forecasts from their web site at http://data-portal.ecmwf.int/. *Chelton et al*.'s [2011b] tracked eddy database was provided by D. Chelton and M. Schlax from their web site at http://cioss.coas.oregonstate.edu/eddies/.

References

Boé, J., A. Hall, and X. Qu (2009), Deep ocean heat uptake as a major source of spread in transient climate change simulations. *Geophys. Res. Lett.*, *36*, L22791, doi:10.1029/2009GL040845.

Böning, C. W., A. Dispert, M. Visbeck, S. R. Rintoul, and F. U. Schwarzkopf (2008), The response of the Antarctic Circumpolar Current to recent climate change. *Nat. Geosci.*, *1*, 864–869.

Chelton, D. B., P. Gaube, M. G. Schlax, J. J. Early, and R. M. Samelson (2011a), The influence of nonlinear mesoscale eddies on oceanic chlorophyll. *Science*, *334*, 328–332.

Chelton, D. B., M. G. Schlax, and R. M. Samelson (2011b), Global observations of nonlinear mesoscale eddies. *Prog. Oceanogr.*, *91*, 167–216.

Ciasto, L. M., and M. H. England (2011), Observed ENSO teleconnections to Southern Ocean SST anomalies diagnosed from a surface mixed layer heat budget. *Geophys. Res. Lett.*, *38*, L09701, doi:10.1029/2011GL046895.

Cunningham, S. A., S. G. Alderson, B. A. King, and M. A. Brandon (2003), Transport and variability of the Antarctic Circumpolar Current in Drake Passage. *J. Geophys. Res.*, *108*, C5, 8084, doi:10.1029/2001JC001147.

Dee, D. P., S. M. Uppala, A. J. Simmons, P. Berrisford, P. Poli, S. Kobayashi, U., et al. (2011), The ERA-Interim reanalysis: configuration and performance of the data assimilation system. *Quart. J. R. Meteorol. Soc.*, *137*, 553–597, doi:10.1002/qj.828.

Fang, F., and R. Morrow (2003), Evolution, movement and decay of warm-core Leeuwin Current eddies. *Deep Sea Res., Part II*, *50*, 2245–2261.

Firing, Y. L., T. K. Chereskin, and M. R. Mazloff (2011), Vertical structure and transport of the Antarctic Circumpolar Current in Drake Passage from direct velocity observations. *J. Geophys. Res.*, *116*, C08015, doi:10.1029/2011JC006999.

Gille, S. T. (2008), Decadal-scale temperature trends in the Southern Hemisphere ocean. *J. Clim.*, *21*, 4749–4765.

Hall, A., and M. Visbeck (2002), Synchronous variability in the Southern Hemisphere atmosphere, sea ice, and ocean resulting from the annular mode. *J. Clim.*, *15*, 3043–3057.

Hanawa, K., P. Rual, R. Bailey, A. Sy, and M. Szabados (1995), A new depth-time equation for Sippican or TSK T-7, T-6 and T-4 expendable bathythermographs (XBT). *Deep Sea Res., Part I*, *42*, 1423–1451.

Hogg, A. M. C., M. P. Meredith, J. R. Blundell, and C. Wilson (2008), Eddy heat flux in the Southern Ocean: Response to variable wind forcing. *J. Clim.*, *21*, 608–620.

Holland, M. M., C. M. Bitz, and E. C. Hunke (2005), Mechanisms forcing an Antarctic Dipole in simulated sea ice and surface ocean conditions. *J. Clim.*, *18*, 2052–2066.

Holland, P. R., and R. Kwok (2012), Wind-driven trends in Antarctic sea ice drift. *Nat. Geosci.*, *5*, 872–875, doi:10.1038/ngeo1627.

Isern-Fontanet, J., E. Garcia-Ladona, and J. Font (2003), Identification of marine eddies from altimetric maps. *J. Atmos. Oceanic Technol.*, *20*, 772–778.

Jacobs, S. S., A. Jenkins, C. F. Giulivi, and P. Dutrieux (2011), Stronger ocean circulation and increased melting under Pine Island Glacier ice shelf. *Nat. Geosci.*, *4*, 519–523.

Jiang, C., S. Gille, J. Sprintall, K. Yoshimura, and M. Kanamitsu (2011), Spatial variation in turbulent heat fluxes in Drake Passage. *J. Clim.*, *25*, 1470–1488.

Kalnay, E., et al. (1996), The NCEP/NCAR 40-year reanalysis project. *Bull. Am. Meteorol. Soc.*, *77*, 437–471.

Kanamitsu, M., W. Ebisuzaki, J. Woollen, S.-K. Yang, J. J. Hnilo, M. Fiorino, and G. L. Potter (2002), NCEP-DOE AMIP-II Reanalysis (R-2). *Bull. Am. Meteorol. Soc.*, *83*, 1631–1643.

Kubota, M., N. Iwasaka, S. Kizu, M. Konda, and K. Kutsuwada (2002), Japanese ocean flux datasets with use of remote sensing observations (J-OFURO). *J. Oceanogr.*, *58*, 213–225.

Kwok, R., and J. C. Comiso (2002), Spatial patterns of variability in Antarctic surface temperature: Connections to the Southern Hemisphere Annular Mode and the Southern Oscillation. *Geophys. Res. Lett.*, *29* (14), 1705, doi:10.1029/GL015415.

Lenn, Y.-D., T. K. Chereskin, J. Sprintall, and E. Firing (2007), Mean jets, mesoscale variability and eddy momentum fluxes in the surface layer of the Antarctic Circumpolar Current in Drake Passage. *J. Mar. Res.*, *65*, 27–58.

L'Heureux, M. L., and D. W. J. Thompson (2006), Observed relationships between El Niño–Southern Oscillation and the extratropical zonal-mean circulation. *J. Clim.*, *19*, 276–287.

Liu, J., J. Curry, and D. G. Martinson (2004), Interpretation of recent Antarctic sea ice variability. *Geophys. Res. Lett.*, *31*, L02205, doi:10.1029/2003GL018732.

Meredith, M. P., and A. M. Hogg (2006), Circumpolar response of Southern Ocean eddy activity to a change in the Southern Annular Mode. *Geophys. Res. Lett.*, *33*, L16608, doi:10.1029/2006GL026499.

Meredith, M. P., E. J. Murphy, E. J. Hawker, J. C. King, and M. I. Wallace (2008), On the interannual variability of ocean temperatures around South Georgia, Southern Ocean: Forcing by El Niño/Southern Oscillation and the Southern Annular Mode. *Deep Sea Res. Part II*, *55*, 2007–2022.

Nan, S., and J. Li (2003), The relationship between summer precipitation in the Yangtze River valley and the previous Southern Hemisphere Annular Mode. *Geophys. Res. Lett.*, *30*, 24, 2266, doi:10.1029/2003GL018381.

Naveira Garabato, A. C., L. Jullion, D. P. Stevens, K. J. Heywood, and B. A. King (2009), Variability of Subantarctic Mode Water and Antarctic Intermediate Water in Drake Passage during the late-twentieth and early-twenty-first centuries. *J. Clim.*, *22*, 3661–3688.

O'Neill, L. W., D. B. Chelton, and S. K. Esbensen (2003), Observations of SST-induced perturbations of the wind stress field over the Southern Ocean on seasonal timescales. *J. Clim.*, *16*, 2340–2354, doi:10.1175/2780.1.

O'Neill, L. W., D. B. Chelton, S. K. Esbensen, and F. J. Wentz (2005), High-resolution satellite measurements of the atmospheric boundary layer response to SST variations along the Agulhas Return Current. *J. Clim.*, *18*, 2706–2723, doi:10.1175/JCLI3415.1.

Orsi, A., T. Whitworth, III, and W. D. Nowlin, Jr. (1995), On the meridional extent and fronts of the Antarctic Circumpolar Current. *Deep-Sea Res., Part I*, *42*, 641–673.

Qiu, B., and K. A. Kelly (1993), Upper-ocean heat balance in the Kuroshio Extension region. *J. Phys. Oceanogr.*, *23*, 2027–2041.

Sokolov, S., and S. R. Rintoul (2009), Circumpolar structure and distribution of the Antarctic Circumpolar Current fronts: 2. Variability and relationship to sea surface height. *J. Geophys. Res.*, *114*, C11019, doi:10.1029/2008JC005248.

Sprintall, J. (2003), Seasonal to interannual upper ocean variability in the Drake Passage. *J. Mar. Res.*, *61*, 27–57.

Sprintall, J. (2008), Long-term trends and interannual variability of temperature in Drake Passage. *Prog. Oceanogr.*, *77*, 316–330.

Stephenson, G. R., S. T. Gille, and J. Sprintall (2012), Seasonal variability of upper ocean heat content in Drake Passage. *J. Geophys. Res.*, *117*, C04019, doi:10.1029/2011JC007772.

Thompson, D. W. J., and J. M. Wallace (2000), Annular modes in the extratropical circulation: Part I. Month-to-month variability. *J. Clim.*, *13*, 1000–1016.

Trenberth, K. E., and T. J. Hoar (1997), El Niño and climate change. *Geophys. Res. Lett.*, *24*, 3057–3060.

Turner, J. (2004), The El Niño–Southern Oscillation and Antarctica. *Int. J. Climatol.*, *24*, 1–31.

White, W. B., and R. G. Peterson (1996), An Antarctic circumpolar wave in surface pressure, wind, temperature, and sea ice extent. *Nature*, *380*, 699–702.

Willis, J. K., D. Roemmich, and B. Cornuelle (2004), Interannual variability in upper ocean heat content, temperature, and thermometric expansion on global scales. *J. Geophys. Res.*, *109*, C12036, doi:10.1029/2003JC002260.

Wolter, K., and M. S. Timlin (1998), Measuring the strength of ENSO—how does 1997/98 rank? *Weather*, *53*, 315–324.

Yu, L., and R. Weller (2007), Objectively analyzed air-sea heat fluxes for the global ice-free oceans (1981–2005). *Bull. Am. Meteorol. Soc.*, *88*, 527–539.

Yuan, X., and D. G. Martinson (2000), Antarctic sea ice extent variability and its global connectivity. *J. Clim.*, *13*, 1697–1717.